




Open Archive Toulouse Archive Ouverte (OATAO)

OATAO is an open access repository that collects the work of Toulouse researchers and makes it freely available over the web where possible

This is an author's version published in: <http://oatao.univ-toulouse.fr/25177>

Official URL: <https://doi.org/10.1108/RPJ-04-2016-0063>

To cite this version:

Perevoshchikova, Nataliya and Rigaud, Jordan  and Sha, Yu and Heilmaier, Martin and Finnin, Barrie and Labelle, Elena and Wu, Xinhua *Optimisation of selective laser melting parameters for the Ni-based superalloy IN-738 LC using Doehlert's design.* (2017) *Rapid Prototyping Journal*, 23 (5). 881-892. ISSN 1355-2546

Any correspondence concerning this service should be sent to the repository administrator: tech-oatao@listes-diff.inp-toulouse.fr

Optimisation of Selective Laser Melting parameters for the Ni-based superalloy IN-738 LC using Doehlert's design

1. Introduction

Selective laser melting (SLM) is of huge interest for production of complex shaped metal parts for gas turbine industry and some nuclear applications [1, 2]. The SLM process is a rapid additive manufacturing technology suited to the net-shape fabrication of high value metallic components with complex shape. This method uses a laser, which scans over and selectively melts metal powder in a powder bed to build 3D components layer by layer to the design in a Computer-Aided Design (CAD) file. SLM provides a potential alternative to the casting process, facilitating more optimal designs in terms of component mass and performance.

The microstructure and grain size resulting from the SLM process is controlled through a large number of key parameters [1, 2] potentially enhancing mechanical properties compared to conventionally cast structures by reducing or eliminating microstructural elements that impair mechanical properties [3, 4]. Despite these advantages, an issue that needs to be addressed using SLM to manufacture metal components for aerospace industry is structural integrity, which is impaired by induced thermal residual stress and micro-cracking as well as micro-pore formation.

1.1 Thermal residual stress

Thermal residual stresses are formed during casting, welding as well as during SLM processes [5, 6, 7]. During SLM, thermal residual stresses are experienced during heating and cooling of molten top layers [6, 7]. The rapid heating of the top layer combined with the relatively low heat conductivity of the material creates a steep temperature gradient. The top layer tends to rapidly expand due to rapid heating putting the cooler lower layer in tension inducing elastic tensile strain. Once the top layer melts, it is stress relieved and the lower layer goes back to being flat. During

cooling, the top layer tends to shrink due to thermal contraction, while the underlying layer tends to expand due to the heat transfer from the melt pool. This causes tensile stresses in the top layer and compressive stresses in the cooler underlying layer creating conditions conducive to hot cracking. A further feature of the SLM process is temperature cycling below the solidus temperature, which additionally contributes to the evolution of thermal residual stresses. If these thermal residual stresses are of sufficient magnitude, they trigger crack formation and propagation in the manufactured parts.

1.2 Micro-cracking in IN 738

IN-738 LC is a low carbon nickel based superalloy which consists of high volume fraction of γ' ($\text{Ni}_3(\text{Al}, \text{Ti})$) intermetallic strengthening phase in the face centred cubic solid solution matrix, γ . Cracking in alloys of type IN-738 typically results from three mechanisms: liquation cracking, strain-age cracking or solidification cracking [8, 9, 10].

Liquation cracking is a type of hot cracking with a liquid phase involved that takes place during the final stages of solidification. Here, liquation involves the formation of a $\gamma+\gamma'$ eutectic below the melting point of the alloy. Liquation can be either constitutional liquation or liquation by segregation.

When temperature increases, γ' particles dissolve progressively. If the temperature reaches the melting point of the γ' phase before it is completely dissolved, the γ' particle melts (constitutional liquation). If the particle dissolves completely before temperature reaches its melting point, no γ' liquation takes place, however, γ' dissolution leads to a local enrichment of the γ matrix in Al and Ti decreasing the melting point at that location [11].

Liquation by segregation is a consequence of elemental segregation during cooling of the alloy. During crystallization the liquid concentration tends to reach the eutectic phase composition decreasing the melting point at that location.

During cooling the γ' particle precipitation and growth at the grain boundaries leads to grain boundary deformation inducing strain and causes strain-age cracking.

Solidification cracking does not occur during casting and SLM and only develops during welding in the final stages of solidification caused by residual stresses (contraction) generated as the weld pool solidifies.

The SLM process uses welding techniques at much higher rates. Therefore, cracking during SLM process is similar to that in welding: liquation cracking and strain-age cracking [12]. In addition, cold cracking occurs below the solidus temperature during cooling when the material is subjected to thermal cycling.

Thermal stresses, micro-cracking and micro-pores can be reduced through control of SLM parameters including heated platforms [6, 7, 12, 13, 34]. Generally, increasing the temperature of the platform can reduce thermal stresses [6, 7]. Cracking sensitivity can be reduced during SLM through the optimisation of the alloy. In order to address cracking sensitivity, it was shown that Si and Mn contents for Hastelloy-X [16] and Si for IN-738 [14, 15] need to be kept as low as possible, but the opposite is the case for increasing mechanical properties [17, 18, 19]. Hot Isostatic Pressing (HIP) can be employed to close pores and cracks and then the microstructure can be improved after HIP using heat treatment [20, 21], however, surface cracks and open porosity may still remain [21].

The objectives of the present work are twofold: first, optimal SLM parameters (power, speed and hatching distance) for IN-738 LC alloy powder, yielding a microstructure with a porosity content of <0.5% and without micro cracks should be found. Second, a successful experimental methodology should be developed that minimises the number of experiments and the time to achieve these optimal SLM parameters. In order to reduce the number of experiments, a Doehlert design approach will be used [22]. This method is widely used in chemistry [23] but application to the optimisation of SLM parameters has not been demonstrated in literature so far. The experimental approach will be exemplified with the Doehlert matrix response variable, relative density, by comparing Archimedes method with microstructural assessments of pores and cracks from image analysis. In addition, utilizing tensile testing of vertically built samples at room temperature the mechanical properties of SLM IN-738 LC followed by standard heat treatment (HT) [25] and by HIP + HT, respectively, will be compared to those of conventionally manufactured cast material [25]. HIP was applied to close possible pores and cracks in SLMed material, particularly cracks, which are strictly prohibited in rotating parts in aeroengines. Slow cooling rate during HIP can cause grain and precipitate growth, HT following the HIP treatment has, thus,

been applied to establish the desired γ/γ' microstructure as expected from the standard heat treatment. As we deliberately restrict ourselves on vertically built samples, this work will not address the impact of anisotropy on mechanical properties.

2. Design of experiments

2.1 Selection of parameters

SLM parameters, such as building method, layer thickness, laser offset, laser type and scanning strategy influence the as-built microstructure [33]. The effects of power (W), scanning speed (mm/s) and hatching distance (mm) on the final microstructure of as-built part are studied in this paper. The hatching distance is the distance between two parallel melt pools scanned closely together as schematically depicted in Fig. 1. These three control parameters are key parameters and interact with each other to influence a key factor in the metal SLM process referred to as the laser energy density, E (J/mm^3) [26]. The laser energy density is given by

$$E = \frac{P}{v \cdot h \cdot t} \quad (1)$$

where, P is laser power (W), v is scanning speed (mm/s), h is hatching distance (mm) and t is layer thickness (mm).

Figure 1

Even though the energy density is a crucial indicator of energy input, it may not be a good indicator to predict the crack and porosity level of SLM processed components [26]. In [12], an obvious decrease in crack size and numbers of SLM IN-738 LC was achieved with low heat input. In [16], microstructure characterization revealed that the pore formation during SLM of Hastelloy-X was triggered by very high scanning speed.

2.2 Statistical design

Doehlert matrices present the advantage of being easily expanded in both the variables space and the experimental space [24]. The combined effects were represented by means of a polynomial model [23] for each parameter. The surface methodology was then applied to represent these effects.

The experimental approach uses Doehlert design [22, 27] to develop a series of experiments to investigate the influence of the three processing parameters (scanning speed, power and hatching distance) and arrive at a set of optimal parameters to meet the component integrity objectives pertaining to porosity and cracking.

An experimental field was defined as $P = 270 - 370$ W, $v = 850 - 2250$ mm/s and $h = 0.09 - 0.13$ mm. Each experiment was performed twice in order to validate the Fisher test and to provide a stronger statistical basis for analysis.

Most physical and chemical phenomena in nature can be represented - to a certain extent - by a segment of a parabola. If this is the case, the result of Doehlert design with three parameters (power, scanning speed and hatching distance) will be a 2nd order equation with 1 constant term, 3 linear terms, 3 interaction terms and 3 square terms:

$$Y = a_0 + a_1X_1 + a_2X_2 + a_3X_3 + a_{11}X_1^2 + a_{22}X_2^2 + a_{33}X_3^2 + a_{12}X_1X_2 + a_{13}X_1X_3 + a_{23}X_2X_3 \quad (2)$$

where X_1 , X_2 , and X_3 are coded factors, and Y is estimated response. In this study, the relative density of sample (ρ , %) is the evaluation indicator of response Y, taking into account the influence of three variables, power (X_1), scanning speed (X_2) and hatching distance (X_3). Each experiment is located by its three coded values.

The coded values and the corresponding experimental values are used to set up the experiments and the model respectively. The experimental values (Z_i) were calculated from the coded values (X_i) using

$$Z_i = Z_{0i} + X_i\Delta Z_i \quad (3)$$

where Z_i is the experimental value, Z_{0i} is the central value, X_i the coded value and ΔZ_i the range.

Coefficients $a_0 \dots a_{23}$ in Eq. 2 were calculated from the vector of experimental response (Y), which is relative density measured by Archimedes method and matrix of coded factors X_1 , X_2 , X_3 using

$$a = (X_t X)^{-1} X_t Y \quad (4)$$

where X_t is the transpose of the X matrix.

Typically, the Doehlert statistical design allows the description of a region around an optimal response and contains k^2+k+1 points for k variables [27]. For three variables, thus, a set of 13 experiments is required and the uniform distribution of the experiments can be mapped in a three-dimensional space, Fig. 2. The 13 experiments are equidistant from a central experiment having the coded values (0,0,0) and are distributed on a sphere with a radius of 1. The coded (X_i) and experimental values (Z_i) of these three variables are listed in Table 1. Locations of 13 experiments in the three-dimensional space, Fig. 2. The coded values and locations of 13 experiments were chosen according to experimental matrix in [36]. The origin of the 14th experiment listed in Table 1 (14th experiment) and plotted in Fig. 2 (dot labelled with number 14) is coming from the difference between experimental design and developing method based on a global maximum search which is the search for highest relative density in the present case. To find the global maximum, firstly, all critical points need to be established, i.e all points where the first derivative of a function $Y(X_1, X_2, X_3)$ in Eq. 2 equals zero. Secondly, the function Y at all critical points and all endpoints of the experimental field has to be evaluated to find the global maximum. One set of coded values (14th experiment) listed in Table 1 and plotted in Fig. 2 corresponds to global maximum of function Y .

The significance of the coefficients in Eq. 2 was evaluated by multiple regression analysis based upon the F-test.

Figure 2

Table 1

3. Materials and experimental procedures

Gas atomized IN-738 LC powder having a size range of 20-70 μm supplied by Carpenter (USA) with chemical composition as detailed in Table 2 was used in the current work. An example of as-received particle morphology is shown in Fig. 3. The powder contains a small number of fine particles.

Table 2

Figure 3

The liquidus temperature of IN-738 LC with the chemical composition listed in Table 2 is 1343 °C and the solidus temperature is 1291 °C (estimated using Thermo-Calc 2015a with the TCNI8-database [28]). SLM processing was conducted under the following conditions: platform temperature was 100 °C, atmosphere was argon gas at 5 bar pressure with an oxygen level maintained at < 0.1 %, build layer thickness was 40 µm and laser spot beam was 100 µm. The chess scanning strategy was used to build all test coupons and is described schematically in Fig. 4. The hatching pattern rotates in each layer by 67 ° for the chess strategy.

Figure 4

Fourteen test coupons with cubical dimensions of 10*10*10 mm were manufactured according to the various combinations of processing SLM parameters shown in Table 1 using the EOSINT M280 machine. Each experiment was then repeated. After building up the coupons by SLM, they were cut off from the substrate plate by electrodischarge (wire cut) machining.

The Archimedes method was employed to measure the relative density of test coupon according to ASTM standard [29]. For this method, the balance Jewel Lab FA2204B with capacity of 220 g and accuracy of ± 0.1 mg was used. All test coupons with as-SLM surfaces were submerged in ethanol in an ultrasonic bath for 10 minutes to clean the surfaces. The mass of each coupon was measured three times in both, air and ethanol. The relative density (%) of coupon at 20 °C and at 1 atm was calculated as follows

$$\rho = \frac{\rho_p}{\rho_{theoretical}} \times 100 \quad (5)$$

where

$$\rho_p = (\rho_{ethanol} - \rho_{air}) \times \frac{m_a}{m_a - m_{ethanol}} + \rho_{air}$$

where $\rho_{theoretical}$ for IN-738 LC is 8177.1 kg/m³ [30]. The density of air (ρ_{air}) at 20 °C and at 1 atm is 1.2754 kg/m³. The ethanol density ($\rho_{ethanol}$) at 20 °C is 789 kg/m³. ρ_p is the coupon density; m_a is the mass of the coupon in air at RT; m_f is the mass of the coupon in ethanol at RT. Error bars are reported based on repeat experimental measurement.

During density measurement using the Archimedes method the formation of bubbles (which is an indication of pores open to the surface of the sample) was not observed. For this reason, the part surface was not sealed with lacquer as recommended in the ASTM standard [29].

All coupons were cut in the middle of the cube and one of the cutting surfaces was prepared for metallographic analysis, as shown in Fig. 5. For each set of parameters in Table 1, two samples were taken. Metallographic samples were prepared using standard metallographic approaches. Samples were examined with a Nikon Eclipse Light Microscope. Optical micrographs were taken gradually across the sample's surface perpendicular to build direction. The relative density of pores and cracks from all surfaces was evaluated using ImageJ software [31]. The final relative density of samples excluding defects was analysed. The error bars reported in the following sections are based on repeat image analysis measurements.

Figure 5

Some of the samples were electrolytically etched in a solution of 10 vol. % oxalic acid with 6Volt and 0.4 Ampere for a duration of 26 seconds and examined with Nikon Eclipse Light Microscope and Backscatter electron detector (BSE) using JEOL 7001F field emission gun scanning electron microscope (FEG SEM).

Tensile samples were built in vertical direction using optimal SLM processing parameters. The samples were built as cylinders of 70 mm height and 9 mm in diameter. After building up the samples by SLM, they were cut off from the substrate plate by electrodischarge (wire cut) machining. The samples were machined to their end contour (M8) after standard solid solution heat treatment in air at 1120 °C for 2 hours with air cool, followed by precipitation hardening heat treatment at 850 °C for

24 hours with air cool. This treatment will be abbreviated HT in what follows. Comparatively, HIP at 1120 °C for 2 hours under 150 MPa in argon with 3°C/min heating and cooling rates was carried out followed by standard heat treatment. A commercial-scale HIP vessel (EPSI, Belgium), using argon as the pressurising gas, was used for HIP. Consequently, these samples are designated HIP+HT.

Tensile testing was performed at room temperature (RT) and a strain rate of $4 \times 10^{-3} \text{ s}^{-1}$ using an Instron 100 kN Model 5982 with an extensometer attached to the gage section for continuously monitoring the strain during the test. Three repeat experiments were performed for vertical samples and the error bars reported in the following sections are based on these repeat experimental measurements.

4. Results and discussion

4.1 Relative density

The relative density with error bars of test coupons built using the SLM processing parameters from Table 1 was evaluated using both, Archimedes method and microstructure image analysis and plotted as a function of energy density (Fig. 6). Additionally, values of relative density measured by Archimedes method and microstructure image analysis are listed in Table 1. The relative density predicted by Eq. 2 for SLM processing parameters from Table 1 is plotted as well in Figure 6. Results demonstrate coherency in prediction. The lowest relative density (black dot ~ 95 %-Archimedes method; black triangle ~ 96 % ImageJ analysis and black square ~95.2 % predicted by Eq. 2) corresponds to power 295 W, scanning speed 2250 mm/s and hatching distance 0.11 mm SLM processing parameters. The highest relative density (red dot ~99.4 % - Archimedes method; red triangle ~99.9 % ImageJ analysis and red square ~99.44 % - predicted by Eq. 2) was obtained for 270 W power, 1084 mm/s scanning speed and 0.09 mm hatching distance. This set of processing parameters corresponds to 70 J/mm^3 energy density. The highest energy density specimen corresponds to 345 W, 850 mm/s and 0.11 mm (with the relative density of blue dot ~99.2 %-Archimedes method; blue triangle ~99.6 % ImageJ analysis and blue square ~ 98.6 % predicted by Eq. 2). The difference between relative densities predicted by the three approaches is in the range of 1 %. From these results it appears that simply maximizing the energy density is not a suitable approach for reducing the

propensity for cracking and pores in SLMed IN-738 LC. Instead, the parameter combinations that yield to energy density around 70 J/mm^3 appears to correspond to the optimal SLM processing window because they provide the highest relative density and lowest level of pore and crack densities.

Figure 6

The complex effect of the three processing parameters on relative density measured by Archimedes method, image analysis and calculated by Eq. 2 is presented in Fig. 7. In order to evaluate the power effect on relative density in isolation, data for a given fixed scanning speed and hatching distance were plotted in Figs. 7e-g. Results of relative density measured by Archimedes method are presented with open circles, image analysis with open triangles and predicted by Eq. 2 with open squares, see Figs. 7a-d. Results of relative density in Figs. 7e-g measured by Archimedes method are presented with full circles, image analysis with full triangles and predicted by Eq. 2 with open squares.

Archimedes method and, particularly microstructure image analysis, demonstrate increase deviation in relative density from low to high scanning speeds, Figs. 7a and b, and from low to high hatching distances, Figs. 7c and d, from about 0.02 % to 4.3 % for image analysis and from about 0.02 % to 0.35 % for Archimedes method suggesting that the reproducibility of the Archimedes method is higher than for the image analysis. The relative density measured by both methods significantly reduces with scanning speed and hatching distance increase, where the opposite is the case in terms of power effect, Figs. 7e-f. The relative densities measured by Archimedes method for high scanning speeds and 0.13 and 0.11 mm hatching distances are improved with power increase and predicted response (Y from Eq. 2) mimics this behaviour. Relative density measured by image analysis demonstrates the same tendency for 0.13 mm hatching distance and shows a result for 0.11 mm hatching distance. Power effect on relative density for 0.11 and 0.13 mm hatching distances is different to those for 0.09 mm, see Fig. 7g. Increasing power reduces relative density as measured by Archimedes method and particularly image analysis, where predicted response Y again mimics this behaviour. Considering that the predicted response Y in Figs. 7e-g agrees well with all experimentally measured data points, we believe that

the trend of reducing the relative density with increasing power for 0.09 mm hatching distance would likely be confirmed by experimental methods.

Figure 7

A relative density of as-built SLM parts of 99.5 % and above is promising and the relative density measured by image analysis lies in this range. However, since image analysis is always performed on 2-dimensional sections of the 3-dimensional microstructure, it may not give an accurate representation of the actual pore and crack distribution in the bulk of the material. Thus, at least the associated scatter during the density measurement is expected to be larger than for the Archimedes method as the latter always takes the whole sample volume into account. The accuracy of relative density measured by Archimedes method can be somewhat compromised by the roughness of the net-finished (SLM) surface, however, the variance in measured density for this method is lower, see Figs. 6 and 7.

Iso-relative density lines calculated with Eq. 2 for hatching distances of 0.09 mm, 0.11 mm and 0.13 mm, respectively, as a function of power and scanning speed are shown in Fig. 8. Only relative densities above 98 % were considered. For 0.09 mm hatching distance, the maximum relative density ~99.4 % determined using the Archimedes method for laser powers in the range from 270 W to 300 W and for scanning speeds from 845 mm/s up to 1225 mm/s, is consistent with the predicted response by Eq. 2, Fig. 8a. This window covers the set of optimal processing parameters predicted by Archimedes method and image analysis. For 0.11 mm hatching distance, at least 99.3 % relative density has been calculated for powers from 270 W to 282 W and for scanning speeds from 845 mm/s up to 900 mm/s, Fig. 8b. Finally, for 0.13 mm hatching distance, at least 98.9 % relative density is predicted for a very narrow processing window, i.e. ranging for the laser power from 271 W to 272 W and for the scanning speed from 850 mm/s to 855 mm/s, see inset in Fig. 8c.

These results suggest that the highest relative density as evaluated by Archimedes method and microstructure image analysis can be obtained in a wide operating window of suitable processing parameters (scanning speed and power, see Fig. 8a) provided the hatching distance is fixed at 0.09 mm. Further, the results also reveal the hatching distance to be a crucial parameter in the set of SLM parameters as the relative density reduces dramatically with an increase in hatching distance. The same

tendency is tracked for power and scanning speed, particularly for scanning speed, whose operating windows are both narrowed with hatching distance increase suggesting that there is the synergy between hatching distance, scanning speed and power.

Figure 8

4.2 Microstructure characterization

Selective Laser Melted and heat treated microstructures

The microstructures of SLM IN-738 LC built with three different combinations of SLM processing parameters are shown in Fig. 9. Optical micrographs were taken systematically from across the sample as schematically shown in Fig. 5 and stitched together. Obviously, only the sample, designated no. 14 in Table 1 and clearly lying with its parameters in the optimal processing window is visibly free of pores and cracks, Fig. 9a. The sample no. 7 processed with power = 345 W, scanning speed = 850 mm/s and hatching distance = 0.11 mm exhibited micro-cracks, Fig. 9b. The sample no. 4 processed with power = 295 W, scanning speed = 2250 mm/s and hatching distance of 0.11 mm exhibited both, micro-pores and micro-cracks, Fig. 9c.

Figure 9

Electrolytic etching of samples as displayed in Fig. 9 reveals some common microstructural features, Fig. 10. Columnar grains are visible and defined by dendrite orientation. The size of melt pool is found to be approximately 100 μm corresponding well to the size of the laser spot beam. The growth direction of grains appears to be along the build direction and along the thermal gradient. Micro-cracks such as the one shown in Fig. 10b where frequently located in the melt pool, whereas micro-pores, Fig. 10c, are usually observed between adjacent melt pools. Fig. 11 details location and propagation of the micro-crack shown in the overview, Fig. 10b, indicating that crack propagation is clearly intergranular.

Figure 10

Figure 11

From these results it appears that the micro-pores are observed in the samples built with high scanning speed (above 1316 mm/s) and large hatching distance. As the pores locate between the melt pools, Fig. 10c, this suggests that the scanning speed is too fast resulting in poor fusion of the melt pool to the previous layer and that a large hatching distance triggers this effect. Lower scanning speeds and a small hatching distance need to be used in optimal parameters providing good overlap between layers. Microcracks occurred due to the material's hot cracking sensitivity where cracks are in the form expected from hot cracking: they are primarily intergranular, see Fig. 11, as this is the path of least resistance. Micro-cracks are observed in the samples built with high power (above 300 W) and high hatching distance (above 0.09 mm) and scanning speed (below 1000 mm/s). The optimal processing parameters provide the reduction of crack formation indicating that these processing parameters reduce the crack sensitivity of material.

The industrial standard heat treatment [25] has been applied to our SLM IN-738 LC sample produced using optimal processing parameters. The microstructure of the SLM sample subjected to the standard heat treatment is shown in Fig. 12. Obviously, the heat treatment strongly influences microstructural features. While the as-SLM material shows melt-pools as exemplified with Figs. 10 and 11, heat treatment erases these melt-pools and the microstructure consists of large γ -matrix columnar grains, Fig. 12a. Inside these γ -grains a bi-modal distribution of fine secondary γ' particles situated between coarser primary γ' precipitates are visible, (see the higher magnification micrograph Fig. 12b). This bimodal particle microstructure compares well with the one observed for as-cast material [32].

Figure 12

4.2 Mechanical properties

Tensile tests were performed on the SLM HT and HIP+HT samples, respectively. Engineering stress-strain curves are plotted in Fig. 13. For each set of experiments, at least 3 tests were performed and these data are plotted in Fig. 13. In Table 3 the tensile test results are summarized and compared with fully heat-treated cast material

[25]. Clearly, the properties from standard cast material were exceeded by the SLM material in terms of both, yield strength (being ~4%-9% higher) and UTS (~27%-33%). More importantly, the average elongation at fracture is doubled as compared with the cast material. Assessing heat-treated SLM samples versus HIP+HT ones yields very similar values for all measured properties, i.e. yield strength, UTS and elongation at fracture. In addition, the consistency of the tensile test data is excellent providing confidence in the uniformity of the heat and HIP treatments. From the tensile properties observed, the HIP treatment has not improved the results significantly.

The relative density of SLMed followed by HT and SLMed followed HIP+HT material measured by Archimedes method is ~99.4 % and 99.8 %, respectively. Walston et al. [35] studied the effect of porosity level in the range from 0.035 % after (HIP+HT) to 1 % (HT) on room-temperature tensile properties of a cast single-crystal Ni-based superalloy. Their results suggest that porosity levels in this range have no effect on tensile properties. The level of porosity in the current material investigation after HT and HIP+HT is the same and is within the porosity range reported by Walston in [35]. Thus, it would be expected also to have no influence on mechanical properties.

It may be concluded that by applying our optimised processing parameters SLM of IN 738 LC the level of pores and cracking can be reduced to the extent that HIP is not necessary in terms of tensile properties sensitivity.

Figure 13

5. Conclusions

SLM processing parameters (power, scanning speed, hatching distance) for IN-738 LC were successfully optimised after only 14 experiments using Doehlert design.

Two methods, Archimedes method and image analysis were used in this study to assess relative density of SLM produced samples with sets of processing parameters as listed in Table 1 show coherency in prediction with predicted response (Y) by Eq. 2.

By using optimised process parameters (low heat input, medium scanning speed and small hatching distance) which provides medium energy density, samples of IN-738

LC with a macroscopic porosity $< 0.5 \%$ and free of micro-cracks can be manufactured by SLM. The synergy between hatching distance, scanning speed and power appears to be significant for micro-pore and micro-crack formation. An obvious decrease in crack and pore numbers of SLM IN-738 LC powder alloy was achieved with reduced hatching distance and reduced scanning speed, and reduced power.

The mechanical properties of SLM IN-738 LC produced using optimal processing parameters followed by standard heat treatment [25] demonstrated superior strength and ductility properties as compared to those of conventionally manufactured cast-material [4]. Additional HIP of SLM material did not yield a noticeable effect on tensile properties indicating that the level of both, porosity and crack density might be acceptable without HIP.

References

- [1] Muktinutalapati, N. R. (2011), "Materials for Gas Turbines – An overview", *Advance in Gas Turbine Technology*, pp. 293-314, InTech.
- [2] Kelbassa, I., Albus, P., Dietrich, J., Wilkes, J. (2008), "Manufacture and repair of Aero engine components using laser technology", *Proceedings of the 3rd Pacific International Conference on Application of Laser and Optics*, pp. 208-212, Beijing, China.
- [3] Linn, S., Scholz, A., Oechsner, M., Berger, C., Luesebrink, O. (2011), "Evaluation of property scatter of Ni-base alloy in 738 LC", *Material Science and Engineering A*, 528 (2011), pp. 4676-4682.
- [4] Mackay, R.A. and Ebert, L.J. (1983), "The development of directional coarsening of the gamma-prime precipitate in superalloy single crystals", *Scripta Metallurgica*, Vol. 17, pp. 1217-1222.
- [5] Dantzig, J.A. and Rappaz, M. (2009), "Solidification", First edition, EPFL Press, Lausanne, Switzerland.
- [6] Mercelis, P. and Kruth, J.-P. (2006), "Residual stresses in selective laser sintering and selective laser melting", *Rapid Prototyping Journal 12*, Iss 5, pp. 254-265.
- [7] Harrison, N.J., Todd, I., Mumtaz, K. (2015), "Reduction of micro-cracking in nickel superalloys processed by Selective Laser Melting: A fundamental alloy design approach", *Acta Materialia*, Vol. 94, pp. 59-68.
- [8] Ojo, O.A. and Chaturvedi, M.C. (2007), "Liquation microfissuring in the weld heat-affected zone of an overaged precipitation-hardened nickel-base superalloy", *Metallurgical and Materials Transactions A*, Vol. 38A, pp. 356-369.
- [9] Ojo, O.A. and Chaturvedi, M.C. (2005), "On the role of liquated γ' precipitates in weld heat affected zone microfissuring of a nickel-based superalloy", *Material Science and Engineering A*, Vol. 403, pp. 77-86.
- [10] Ojo, O.A., Richards, N.L. and Chaturvedi, M.C. (2006), "Study of the fusion zone and heat-affected zone microstructures in tungsten inert gas-welded INCONEL 738LC superalloy", *Metallurgical and Materials Transactions A*, Vol. 37A, pp. 421-433.

- [11] Tancret, F. (2007), "Thermocalc and Dictra simulation of constitutional liquation of gamma prime during welding of Ni based superalloys", *Computational Materials Science*, Vol. 41, pp. 13-19.
- [12] Zhong, M., Sun, H., Liu, W., Zhu, X., He, J. (2005), "Boundary liquation and interface cracking characterization in laser deposition of Inconel 738 on directionally solidified Ni-based superalloy", *Scripta Materialia*, Vol. 53, pp. 159-164.
- [13] Carter, L.N., Martin, C., Withers, P.J., Attallah, M. (2014), "The influence of the laser scan strategy on grain structure and cracking behaviour in SLM powder-bed fabricated nickel superalloy", *Journal of Alloys and Compounds*, Vol. 615, pp. 338-347.
- [14] Engeli, R., Etter, T., Meidani, H. (2015), "Gamma prime precipitation strengthened nickel-based superalloy for use in powder based additive manufacturing process", *Patent EP2886225 A1*.
- [15] Engeli, R., Etter, T., Geiger, F., Stankowski, A., Wegener, K. (2015), "Effect of Si on the SLM processability of IN738LC", *Solid Freeform Fabrication Symposium*, pp. 823. Austin, Texas, USA.
- [16] Tomus, D., Jarvis, T., Wu, X., Mei, J., Rometsch, R., Hery, E., Rideau, J.-F., Vaillant, S. (2013), "Controlling the microstructure of Hastelloy-X components manufactured by Selective Laser Melting", *Physics Procedia*, Vol. 41, pp. 823-827.
- [17] Zhu, Y., Zhang, S., Zhang, T., Zhang, J., Hu, Z., Xie, X. and Shi, C. (1992), "A new way to improve the superalloys", *Superalloys 1992*, The Minerals, Metals & Materials Society, Warrendale, PA, pp. 145-154.
- [18] Holt, R.T. and Wallace, W. (1976), "Impurities and trace elements in nickel-based superalloys", *International Metals Reviews*, Vol. 203, pp. 1-24.
- [19] Decker, R.F. and Freeman, J.W. (1957), Report 57, *Engineering Research Institute, the The University of Michigan*.
- [20] Kunze, K., Etter, T., Grässlin, J., Shklover, V. (2015), "Texture, anisotropy in microstructure and mechanical properties of IN738LC alloy processed by selective laser melting (SLM)", *Materials Science and Engineering A*, Vol. 620, pp. 213-222.
- [21] Rickenbacher, L., Etter, T., Hövel, S. and Wegener, K. (2013), "High temperature material properties of IN738LC processed by selective laser melting (SLM) technology", *Rapid Prototyping Journal*, Vol. 19, Iss 4, pp. 282-290.

- [22] Doehlert, D.H. (1970), "Uniform shell designs", *Applied Statistics*, Vol. 19, pp. 231-239.
- [23] Taragano, V.M. and Pilosof, A.M.M. (1999), "Application of Doehlert designs for water activity, pH and fermentation time optimization for *Aspergillus niger* pectinolytic activities production in solid-state and submerged fermentation", *Enzyme and Microbial Technology*, Vol. 25, pp. 411-419.
- [24] Quignon, F., Huyard, A., Schwartzbrod, L. et al. (1997), "Use of Doehlert matrices for study of poliovirus-1 adsorption", *Journal of Virological Methods*, Vol. 68, pp. 33-44.
- [25] Alloy IN-738 Technical Data, The International Nickel Company, INC., One New York Plaza, New York, N.Y. 10004.
- [26] Gu, H., Gong, H., Pal, D., Rafi, K., Starr, T., Stucker, B. (2013), "Influences of energy density on porosity and microstructure of selective laser melted 17-4PH stainless steel" *Solid Freeform Fabrication Symposium-An additive Manufacturing conference*, pp. 474-489, Austin, Texas, USA.
- [27] Karima, K. (2008), Ph.D thesis, University Mentouri Constantine, Algeria.
- [28] Andersson, J.O., Helander, T., Höglund, L., Shi, P.F., Sundman, B. (2002), *Computational tools for materials science*. Calphad, Vol. 26, pp. 273-312.
- [29] ASTM B962-13, 2014, USA.
- [30] Limkitjaroenporn, P., Kaewkhao, J., Asavavisithchai, S. (2013), "Determination of mass attenuation coefficients and effective atomic numbers for Inconel 738 alloy for different energies obtained from Compton scattering", *Annals of Nuclear Energy*, Vol. 53, pp.64-68.
- [31] Schneider, C.A., Raband, W.S., Eliceiri, K.W. (2012), "*NIH Image to ImageJ: 25 years of image analysis*", *Nat Methods*, Vol. 9, pp. 671-675.
- [32] Stevens, R.A., Flewitt, P.E. (1981), "The dependence of creep rate on microstructure in a γ' strengthened superalloy", *Acta Metallurgica*, Vol. 29, pp. 867-882.
- [33] Kruth, J.-P., Badrossamay, M., Yasa, E., Deckers, J., Thijs, L., Van Humbeeck, J. (2010), "Part and material properties in selective laser melting of metals", *16th International Symposium on Electromachining*, China.

[34] Cloots, M., Uggowitzer, P. J., Wegener, K. (2016), "Investigations on the microstructure and crack formation of IN738LC samples processed by selective laser melting using Gaussian and doughnut profiles", *Materials and Design*, Vol. 89, pp. 770-784.

[35] Walston, W.S., Bernstein, I.M., Thompson, A.W. (1991), "The role of the γ/γ' eutectic and porosity on the tensile behavior of a single-crystal nickel-base superalloy", *Metallurgical Transactions A*, Vol. 22A, pp. 1443-1451.

[36] Lundstedt, T., Seifert, E., Abramo, L., Thelin, B., Nyström, Å., Pettersen, J., Bergman, R. (1998), "Experimental design and optimization", *Chemometrics and Intelligent Laboratory Systems*, Vol. 42, pp. 3-40.

Optimisation of Selective Laser Melting parameters for IN-738 using Doehlert's design

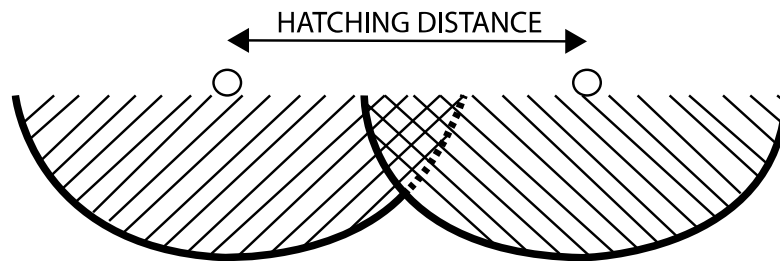


Figure 1 : Schematic describing the hatching distance between two parallel melt pools.

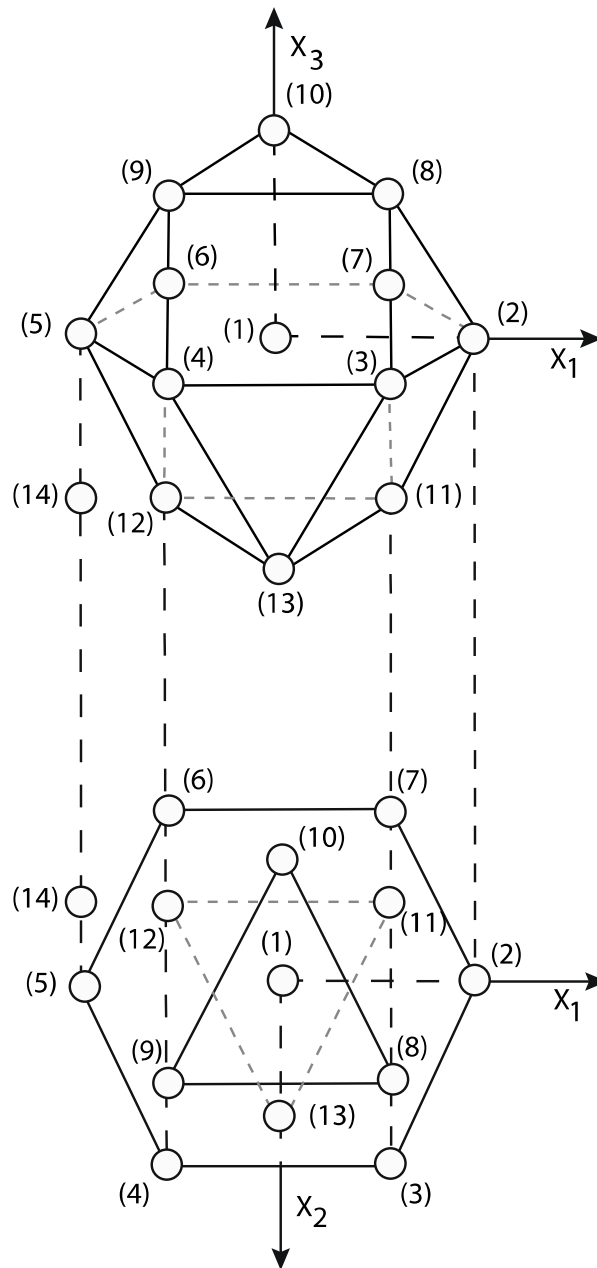


Figure 2: Three-dimensional geometry of experimental space with 13 experimental points for three different coded variables (e.g. X_1 , X_2 and X_3). The bottom figure shows the projection of X_3 axis on X_1 and X_2 , 2-dimension space.

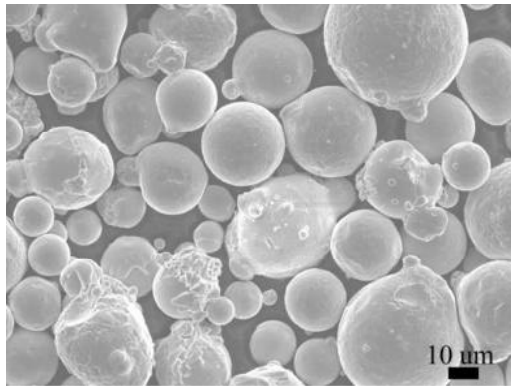


Figure 3: Morphology of gas atomised powder particles.

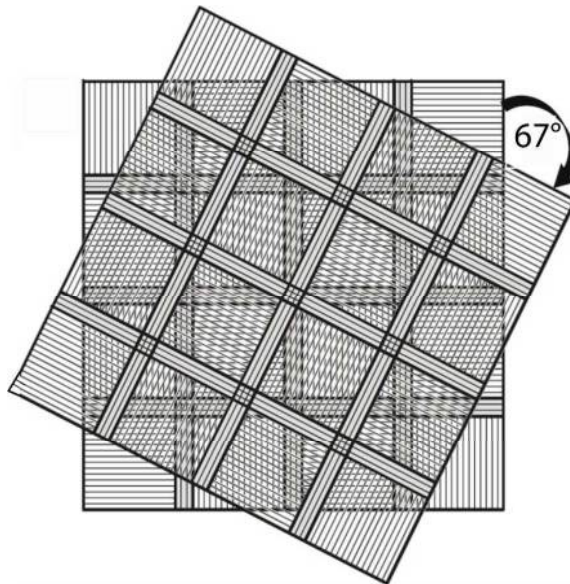


Figure 4: Schematic diagram describing chess scanning strategy.

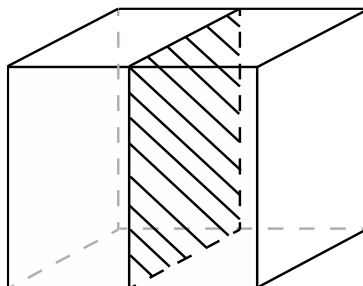


Figure 5: Schematic of SLM built cubes. The hatched area was prepared for metallographic analysis.

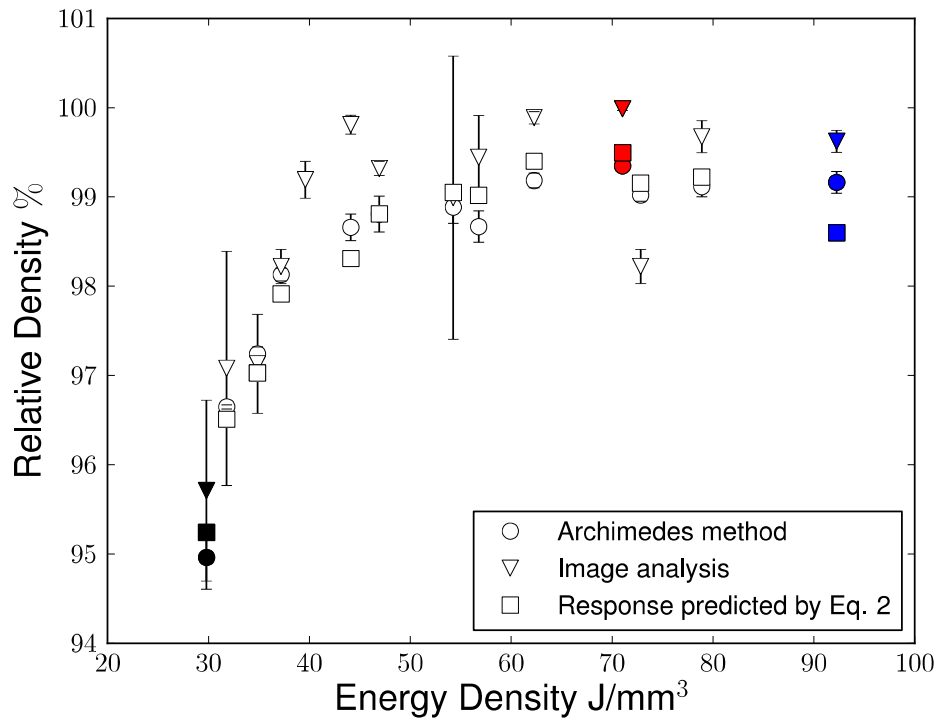
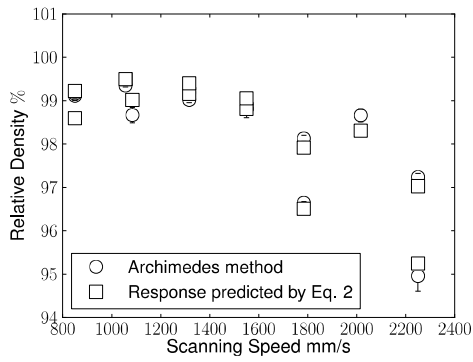
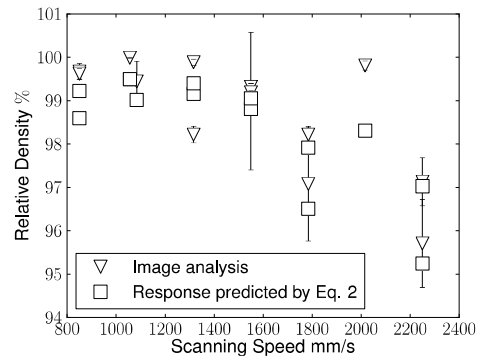


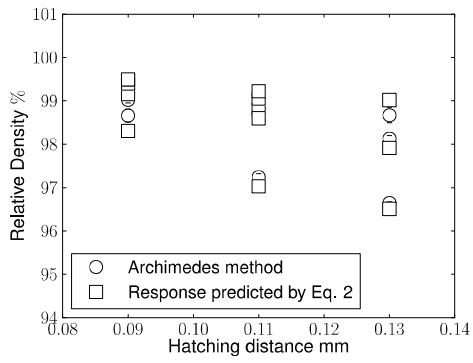
Figure 6: Relative density of samples built using SLM processing parameters from Table 1 versus energy density calculated according to Eq. 1. Circles represent data from Archimedes method, triangles refer to image analysis using ImageJ software and squares represent response predicted (Y) by Eq. 2. Black full symbols correspond to the lowest relative density; red full symbols to the highest relative density; blue full symbols represent the highest energy density.



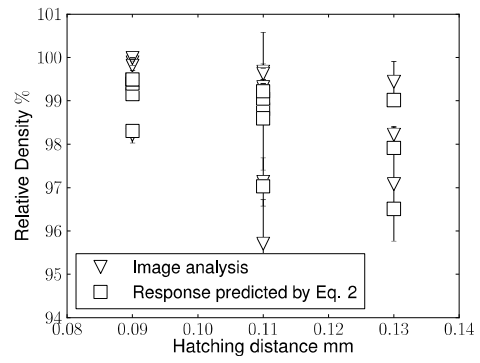
(a)



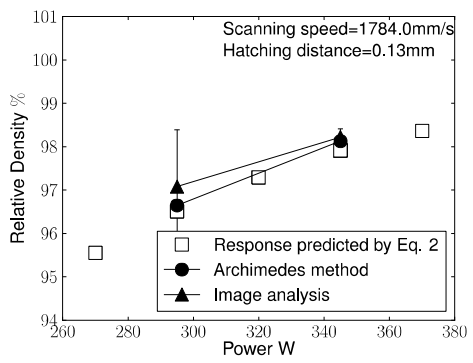
(b)



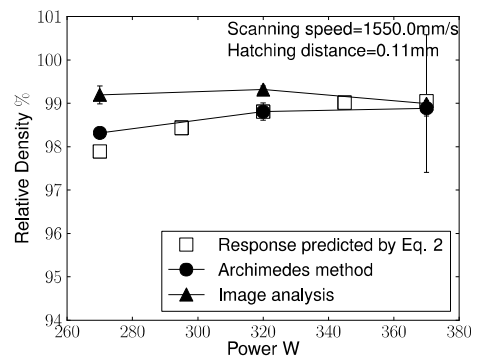
(c)



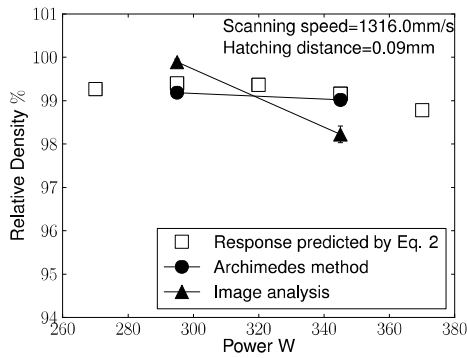
(d)



(e)

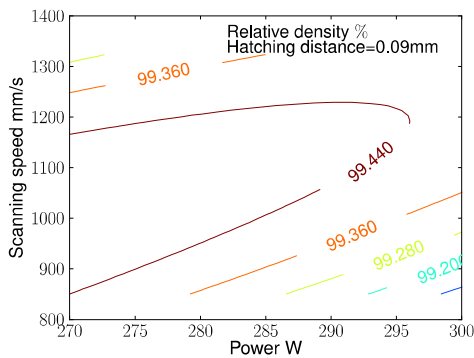


(f)

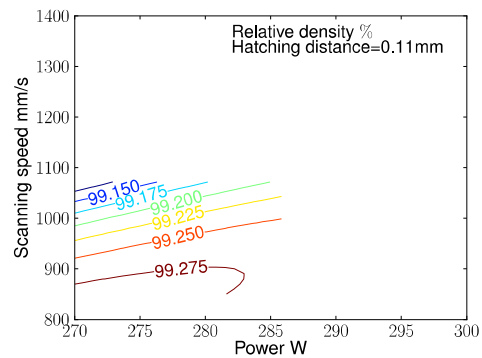


(g)

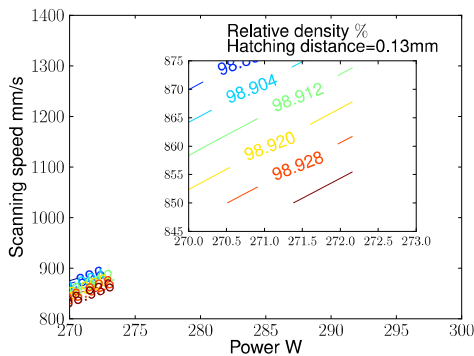
Figure 7: Relative density of samples built using SLM processing parameters from Table 1 measured (circles) using Archimedes method and (triangles) image analysis using ImageJ software, and calculated with response predicted by Eq. 2 (squares) as a function of (a-b) scanning speed and (c-d) hatching distance and (e-g) power. Data of relative density versus power is presented with fixed scanning speed and hatching distance.



(a)



(b)



(c)

Figure 8: Iso-relative density lines calculated with Eq. 2 for (a) 0.09 mm, (b) 0.11 mm and (c) 0.13 mm hatching distances as a function of power and scanning speed.

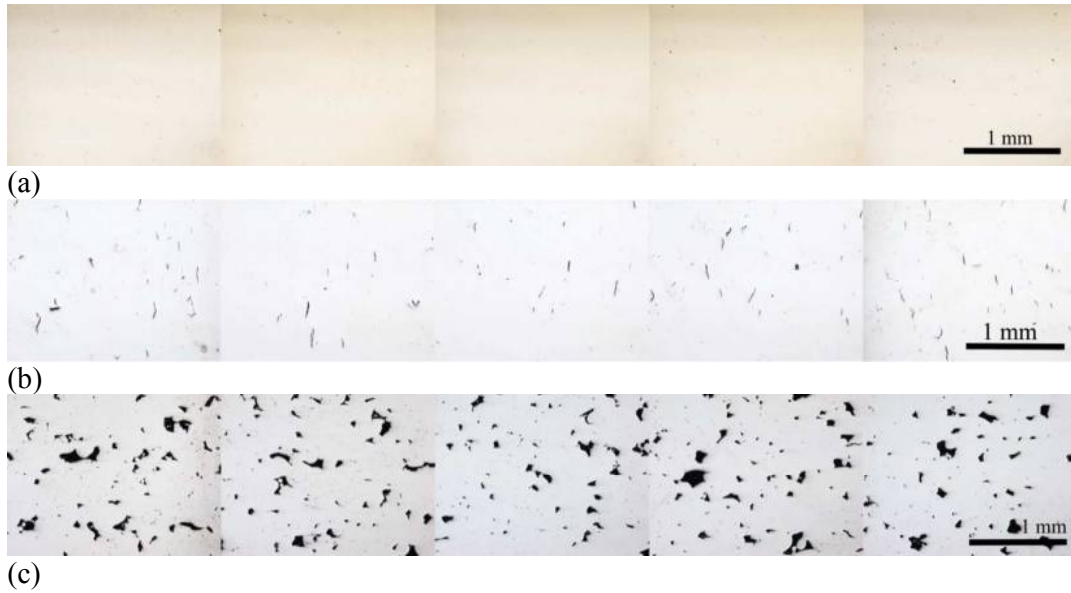
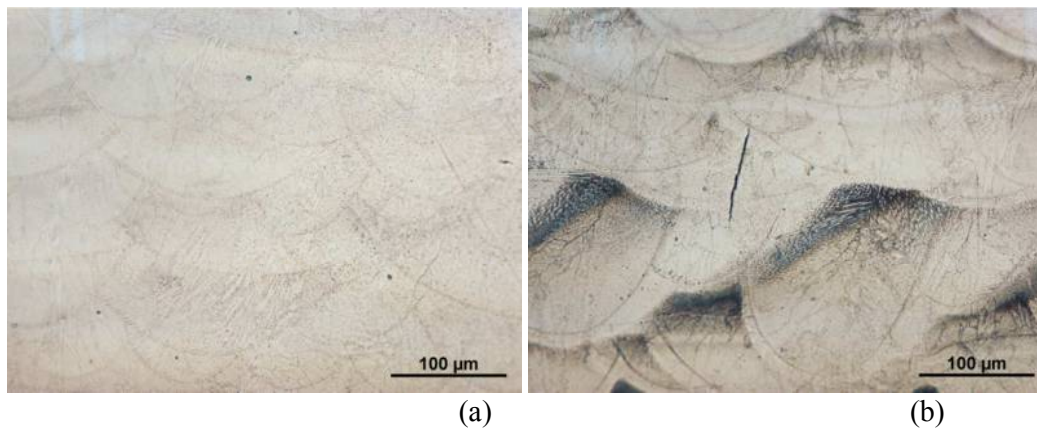
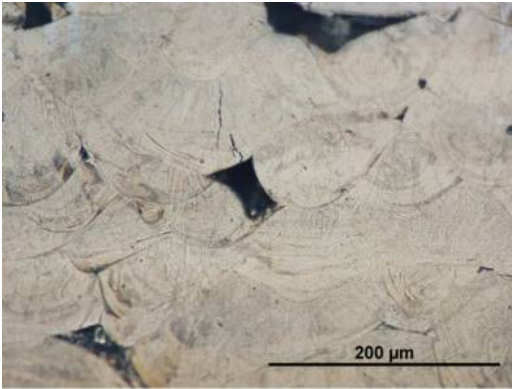


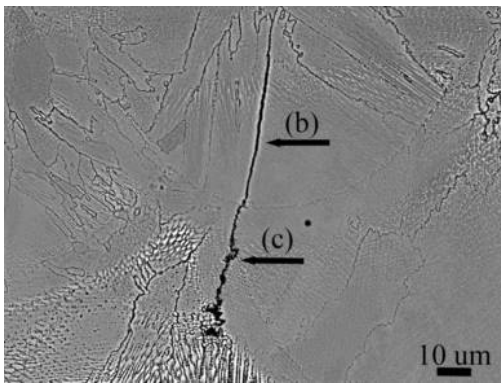
Figure 9: Optical micrographs of ground and polished surfaces of IN-738 LC (a) 270 W, 1084 mm/s and 0.09 mm; (b) 345 W, 850 mm/s and 0.11 mm and (c) 295 W, 2250 mm/s and 0.11 mm SLM processing parameters.



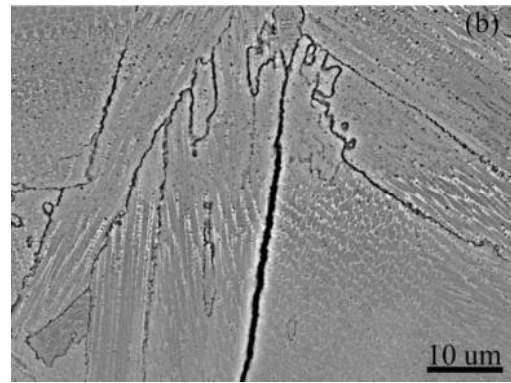


(c)

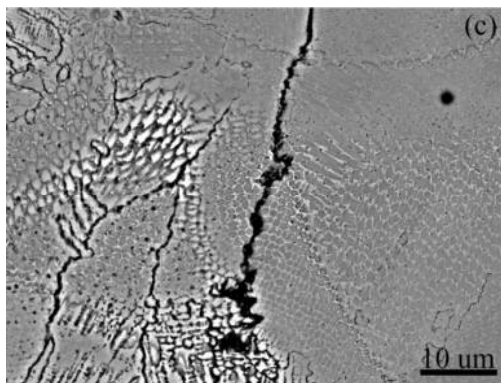
Figure 10: Optical micrograph of electrolytically etched surface of IN-738 LC (a) 270 W, 1084 mm/s and 0.09 mm; (b) built with 345 W, 850 mm/s and 0.11 mm and (c) 295 W, 2250 mm/s and 0.11 mm SLM processing parameters.



(a)



(b)



(c)

Figure 11: Backscatter electron image of electrolytically etched surface of IN-738 LC built with 345 W, 850 mm/s and 0.11 mm SLM processing parameters: (a) low magnification; (b-c) high magnification.

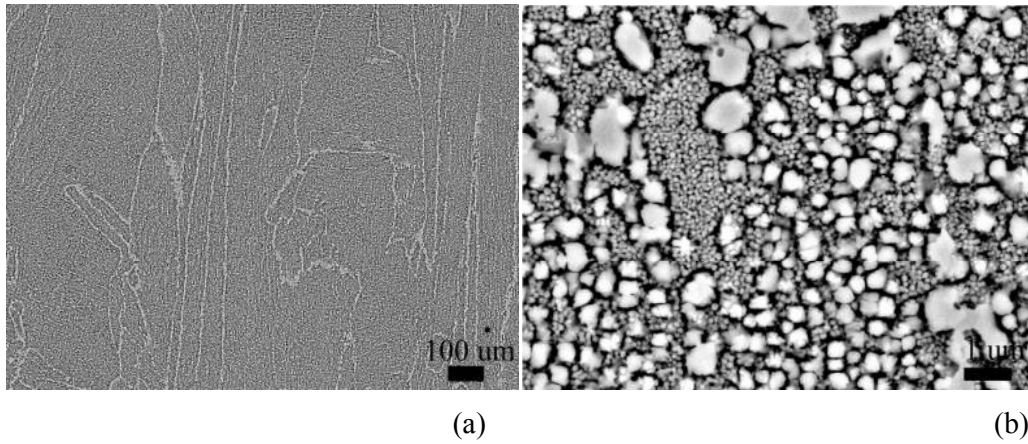


Figure 12: Backscatter electron image of electrolytically etched surface of IN-738 LC produced by SLM and built up in vertical direction followed by standard heat treatment (a) low magnification (b) high magnification.

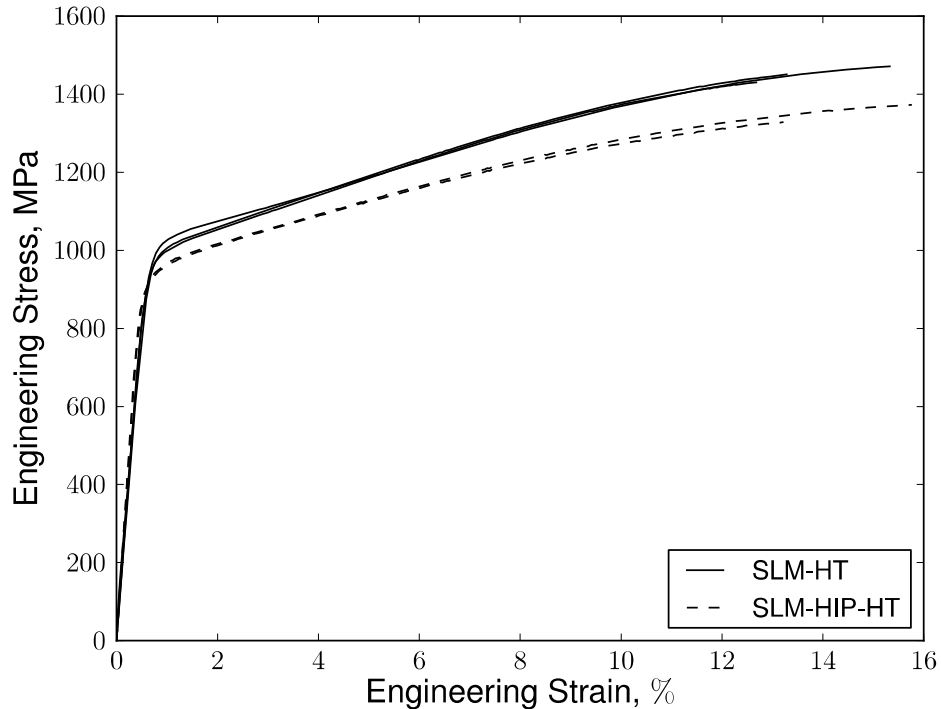


Figure 13: Engineering stress-strain curve for the SLM processed IN738-LC built in vertical direction followed by heat treatment and SLM followed by HIP and heat treatment.

Table 1: Experimental matrix created by the Doehlert design method for free variables, experimental variables and relative density measured by Archimedes method and microstructure image analysis.

Experiment	Coded values			Experimental values			Relative density, %	
	X ₁	X ₂	X ₃	Power, W	Speed, mm/s	Hatching distance, mm	Archimedes method	Image analysis
1	0	0	0	320	1550	0.11	98.84	99.32
2	1	0	0	370	1550	0.11	98.86	98.99
3	0.5	0.866	0	345	2250	0.11	97.24	97.13
4	-0.5	0.866	0	295	2250	0.11	95.3	95.71
5	-1	0	0	270	1550	0.11	98.32	99.19
6	-0.5	-0.866	0	295	850	0.11	99.17	99.67
7	0.5	-0.866	0	345	850	0.11	99.16	99.62
8	0.5	0.289	0.816	345	1784	0.13	98.13	98.22
9	-0.5	0.289	0.816	295	1784	0.13	96.65	97.08
10	0	-0.577	0.816	320	1084	0.13	98.67	99.45
11	0.5	-0.289	-0.816	345	1316	0.09	99.02	98.22
12	-0.5	-0.289	-0.816	295	1316	0.09	99.18	99.89
13	0	0.577	-0.816	320	2016	0.09	98.66	99.81
14	-1	-0.577	-0.816	270	1084	0.09	99.35	99.99

Table 2: Chemical composition of IN738LC used in the current work.

	Ni	Cr	Co	Ti	Al	C	W	Ta	Mo	Nb
wt. %	Bal.	16	8.64	3.46	3.4	0.11	2.58	1.81	1.82	0.99
	Fe	Mn	Si	B	S	Cu	Zr	O	N	H
wt. %	0.08	<0.01	0.04	0.01	0.002	0.01	0.03	0.0169	0.0034	>0.005

Table 3: Engineering tensile properties of cast and SLM processed IN738-LC followed by standard heat treatment at room temperature.

Description	$\sigma_{0.2}$, MPa	σ_{UTS} , MPa	$\epsilon_{uniform}$, %
Cast reference	896	1034	7
SLM-HT: vertical	981±12	1450±16	14±1.1
SLM-HIP-HT:vertical	932±4	1350±22	14±1.3